Distinct classes of antidepressants commonly act to shape pallidal structure and function in mice

Yoshifumi Abe [1], Yuki Sugiura [2, 3], Rae Maeda [2], Shu Taira [4], Keisuke Yoshida [5], Daisuke Ibi [6], Kenji Hashimoto [7], Sho Yagishita [8], and Kenji F Tanaka [1,3,*]

[1] Division of Brain Sciences, Institute for Advanced Medical Research, Keio University School of Medicine, Tokyo, 160-8582, Japan.

[2] Multiomics Platform, Center for Cancer Immunotherapy and Immunobiology, Kyoto University Graduate School of Medicine, Kyoto 606-8501, Japan.

[3] Human Biology-Microbiome-Quantum Research Center (WPI-Bio2Q), Keio University, Tokyo, 160-8582, Japan

[4] Faculty of Food and Agricultural Sciences, Fukushima University, Kanayagawa, Fukushima 960-1296, Japan

[5] Department of Medical Chemistry, Graduate School of Pharmacy, Meijo University, Nagoya 468-8503, Japan

[6] Department of Chemical Pharmacology, Graduate School of Pharmacy, Meijo University, Nagoya 468-8503, Japan

[7] Division of Clinical Neuroscience, Chiba University Center for Forensic Mental Health, Chiba 260-8670, Japan

[8] Laboratory of Structural Physiology, Center for Disease Biology and Integrative Medicine, Faculty of Medicine, The University of Tokyo, Tokyo, 113-0033, Japan.

*Corresponding author
Kenji F Tanaka
35 Shinanomachi, Shinjuku, Tokyo 160-8582, Japan
Phone: +81-3-5363-3934
E-mail address: kftanaka@keio.jp

Running title:

Shared structural footprints of antidepressants.

Abstract

Antidepressants, including selective serotonin reuptake inhibitors (SSRIs), ketamine, and psilocybin, are effective for treating depression despite their distinct modes of action. We hypothesized that their underlying mechanisms of action are shared. Mice were administered escitalopram (15 mg/kg daily for 3 weeks, 21 mice), R-/S-/racemic ketamine (10 mg/kg, single injection, 21–22 mice), or psilocin (1 mg/kg, single injection, 22 mice). Electroconvulsive stimulation (9 times for 3 weeks, 12 mice) and saline were used as controls. After structural magnetic resonance imaging (MRI) of fixed brains, voxel-based morphometry was conducted to assess brain-wide volumetric changes. A single dose of ketamine or psilocin was sufficient to induce MRI-detectable volume changes. All antidepressants increased the volume in the nucleus accumbens, ventral pallidum, and external globus pallidus and decreased the volume in the mediodorsal thalamus, which is distinct from the changes observed with electroconvulsive stimulation. We identified microstructural and molecular changes using super-resolution microscopy and imaging mass spectrometry, respectively. Pallidal volumetric increases were associated with hypertrophy of striatal medium spiny neuron terminals and increased γ-aminobutyric acid (GABA) content. We experimentally addressed whether the overexpression of the vesicular GABA transporter (VGAT) reproduced these changes. The overexpression of striatal VGAT reproduced these structural changes. R-ketamine, SR-ketamine, and psilocin induced more pronounced ventral pallidum hypertrophy, and SSRIs and S-ketamine induced globus pallidus hypertrophy. We discovered shared pallidum-centered structural and molecular changes among various antidepressants, which possibly potentiate the striato-pallidial inhibition associated with antidepressant action. Our data support visualizing antidepressant responses using pallidum-centered GABA MR spectroscopy or structural MRI.

Introduction

Antidepressants are a substantial therapeutic option for major depressive disorder, and first-line treatments, including selective serotonin reuptake inhibitors (SSRIs), are used. SSRIs immediately block serotonin (5-HT) transporters and enhance 5-HT signaling, but long-term SSRI use is necessary [1]. By contrast with classical antidepressants, the dissociative anesthetic ketamine (*N*-methyl-D-aspartate receptor antagonist) [2, 3] and the psychedelic psilocybin (5-HT_{2A} receptor agonist) [4] have recently been recognized as rapid-acting antidepressants offering long-term effects from a single dose. Although the primary pharmacological targets and temporal modes of action differ among these types of antidepressants, they can similarly induce recovery states in patients with major depressive disorder, indicating common underlying mechanisms for the induction and maintenance of recovery. The present study aimed to reveal the shared mechanism of action among different classes of antidepressants.

The acquisition of a recovery state can be understood as an outcome of plastic changes in the brain from a diseased state to a healthy state after treatment. Such brain state changes likely involve unidentified cellular changes, functional plastic changes in the circuitry, and structural plastic changes. Because structure always correlates with function, we hypothesize that identifiable structural plasticity should accompany theoretical functional plasticity. Our strategy involved screening for brain regions undergoing structural plastic changes using structural magnetic resonance imaging (MRI), followed by closer inspection of those regions with super-resolution microscopy (SRM) to identify specific structural plastic changes.

Using this strategy, we studied mice treated with SSRIs, ketamine, and psilocin (the active metabolite of psilocybin). We revealed that all antidepressants were associated with increases in pallidum volume, hypertrophy of vesicular γ-aminobutyric acid (GABA) transporter (VGAT)-positive terminals of striatal medium spiny neurons (MSNs), and increased GABA content in these terminals. Additional volumetric and histological analyses indicated that antidepressants can be divided into two subtypes. We found that the ventral pallidum (VP) and mediodorsal thalamus (MD) were hubs for volumetric changes. Therefore, the nucleus accumbens (NAc)–VP–MD axis was highlighted as an antidepressant action-related circuitry. We also found that antidepressant treatment increased dopamine levels in the basal ganglia.

Methods and Materials

Animals

All animal procedures were conducted in accordance with the National Institutes of Health Guide for the Care and Use of Laboratory Animals and approved by the Animal Research Committee of Keio University School of Medicine (A2022-029). Experiments were performed using 8- to 20-week-old male C57BL/6J mice. All mice were maintained on a 12-h/12-h light/dark cycle (lights on at 08:00), and behavioral experiments were conducted during the light phase. C57BL/6J mice (8 weeks old) were purchased from Oriental Yeast Co., Ltd. (Tokyo, Japan).

Antidepressant treatment

Psilocin was synthesized within the Japanese law according to the methods published by Shirota et al.[5], and its purity was verified by nuclear magnetic resonance analysis (Avance III 600, Bruker, MA, USA). R-ketamine and S-ketamine were prepared by recrystallization of RS-ketamine (Ketalar®, ketamine hydrochloride, Daiichi Sankyo Pharmaceutical Ltd., Tokyo, Japan), as described previously[6]. Escitalopram was used in the SSRI experiments and was purchased from Tokyo Chemical Industry Co., Ltd. (Tokyo, Japan). Psilocin, ketamine, and escitalopram were dissolved in saline.

Mice received a single acute intraperitoneal (i.p.) injection of vehicle, psilocin, SR-ketamine, R-ketamine, or S-ketamine. On the basis of previous studies[7-9], the dose was 1 mg/kg for psilocin and 10 mg/kg for R-ketamine or S-ketamine. RS-ketamine was mixed using 5 mg/kg of R-ketamine and 5 mg/kg of S-ketamine. The mice were perfused 1 week after a single injection with vehicle, psilocin, or ketamine. Escitalopram (15 mg/kg per day in deionized water) or vehicle was delivered by oral gavage for 3 weeks [7]. The mice were perfused 1 day after the final administration of escitalopram.

ECS

The procedure was previously described [10]. Briefly, ECS was administered to mice that were anesthetized with 3.0% sevoflurane once daily for 3 weeks (three times per week, for a total of nine ECS sessions). ECS was administered in square wave pulses of 25 mA and 0.5 msec pulse width for 1 second at a frequency of 100 Hz via bilateral ear clip electrodes (UgoBasile, Comerio, Italy). The control mice underwent the same procedure on the same schedule

without electrical stimulation. The mice were perfused 1 day after the final ECT administration.

Plasmid construction and adeno-associated virus (AAV) preparation

For AAV vector production, we prepared the following construct: pAAV-hSyn-ALFA (SRLEEELRRRLTE)-VGAT-pA[11]. AAVs were produced and their titers were measured. In brief, plasmids for the AAV vector, pHelper (Stratagene, San Diego, CA, USA) and RepCap5 (Applied Viromics, Fremont, CA, USA), were transfected into HEK293 cells (AAV293, Stratagene). After 3 days, the cells were collected and AAVs were purified twice using iodixanol. The AAV titers were estimated using quantitative PCR. The following AAV vector was used in the experiments: AAV_5-hSyn-ALFA-VGAT-pA (2×10^{13} GC/mL).

Viral vector injection

AAVs were injected into wild-type mice. Mice were anesthetized with a mixture of ketamine and xylazine (i.p., 100 mg/kg and 10 mg/kg, respectively) and fixed in a stereotaxic apparatus (Narishige, Tokyo, Japan). The skull surface was exposed, and the periosteum and blood were removed. Next, 0.2 μL of viral solution was injected into the right dorsal striatum through a small hole (+0.6 mm anteroposterior and ±2.2 mm mediolateral from bregma and −2.2 mm dorsoventral from the brain surface according to the atlas of Paxinos and Franklin) using a glass micropipette connected to a Nanoliter 2020 injector (World Precision Instruments, FL, USA). The mice were perfused 3 weeks after AAV injection.

MRI

The procedures used in the *ex vivo* MRI study were previously described[10, 11]. Mice were deeply anesthetized with a mixture of 0.3 mg/kg medetomidine, 4 mg/kg midazolam, and 5 mg/kg butorphanol and perfused with a 4% paraformaldehyde phosphate buffer solution. The brains were removed along with the skull and postfixed in the same fixative for 24 h. The fixed brains were then stored in PBS for 1 week. The duration of paraformaldehyde and PBS immersion was consistent for all samples to avoid differences in brain volumes caused by postperfusion immersion fixation and storage [12]. Brains within their skulls were firmly fixed using fitted sponges into an acrylic tube (22-mm diameter) filled with Fluorinert (Sumitomo 3M Limited, Tokyo, Japan) to minimize the signal intensity attributable to the embedding medium. Additionally, vacuum degassing was performed to reduce air bubble-derived

artifacts in the structural images. The MRI study was performed with an 11.7 T BioSpec 117/11 US/R unit (Biospin GmbH, Ettlingen, Germany) and a volume-type coil with a 23-mm inner diameter for transmitting and receiving. For brain volumetric analysis, the structural images were acquired using T2-weighted multi-slice rapid acquisition with relaxation enhancement (RARE) with the following parameters: repetition time=2000 ms, echo time=75 ms, spatial resolution=100×100×100 μm, RARE factor=32, and averages=8. The structural images after treatment with saline, psilocin, ketamine, and SSRIs were obtained in the current study, and those of brains with ECT treatment and controls were obtained from a previous study using the same protocol[10] and were reanalyzed in this study.

Voxel-based morphometry analysis

Image preprocessing and statistical analysis for the whole-brain voxel-based analysis were performed using SPM12 (Wellcome Trust Centre for Neuroimaging, London, UK) and in-house software written using MATLAB (MathWorks, Natick, MA, USA). First, each T2-weighted image was resized by a factor of 10 to account for the whole-brain volume differences between humans and rodents and aligned to the same space by registering each image to tissue probability maps. Next, each image was segmented into gray matter, white matter, and cerebrospinal fluid using a unified segmentation approach, which enabled image registration, tissue classification, and bias correction. The segmented images were spatially normalized into a study-specific template that was created with all data using a Diffeomorphic Anatomical Registration Through Exponentiated Lie Algebra (DARTEL) algorithm. Modulated gray matter images were then obtained for each animal by the determinant of the Jacobian of the transformation to account for the expansion and/or contraction of the brain regions. These images were smoothed with a 3-mm full width at half maximum Gaussian kernel. The total brain volume was defined as a sum of the gray matter volume (GMV) and the white matter volume.

Whole-brain voxel-wise comparisons of the GMV between each treated mouse and its control were performed using SPM12 with the total brain volume as a covariate. The first analysis compared the GMV between antidepressant- or ECS-treated mice and control mice. The significance threshold for the voxel-wise whole-brain analysis was set at a cluster-level family-wise error corrected p value < 0.05, with an individual voxel threshold of an uncorrected p value $= 0.001$. The significant clusters were overlayed on the study-specific template.

Clustering of volumetric changes was performed by principal component analysis. Statistical t-values were calculated from comparisons of the brain volume values of each defined subregion (see below) between antidepressant-treated mice and control mice. The t-values across the defined subregions were used for principal component analysis.

ROI-based structural covariance analysis

To define ROIs of brain subregions, we utilized the Turone Mouse Brain Template and Atlas [13], which is available at https://www.nitrc.org/projects/tmbta_2019/, and modified the brain subregions. A total of 397 brain subregions were defined in each hemisphere. This atlas was registered to the study-specific mouse T2 template using Advanced Normalization Tools (https://github.com/ANTsX/ANTs). The brain volumes of each defined subregion were estimated by averaging the voxel values (the determinant value of the Jacobian transformation) of the ROI.

Structural covariance analysis was performed using the NBS toolbox (https://www.nitrc.org/projects/nbs/) by reference to previous studies [14-16]. Structural covariance was quantified using the partial correlation coefficient between paired brain volume value estimates across each antidepressant group. This approach yielded a separate connectivity matrix with dimensions of 794×794 for each group that quantified the connectivity strength between all pairs of regions (Fig. 5A). These structural covariances were subjected to Fisher transformation to obtain the z-transformed values. The delta value was calculated by dividing the difference in z-values by the standard deviation (SD) of the difference in z-values. This calculation was performed independently for each pair of regions. The SD of the difference in z-values was estimated by bootstrapping the sample 1000 times. Edges in the network matrices that were 2.5 or more times the SD were identified as suprathreshold. The threshold of SD $\geq$ 2.5 is equal to $p < 0.05$ because the difference in z-values follows a normal distribution. The identified regions were overlayed on the mouse template brain (Fig. 5B). To evaluate the characteristics of the extracted network, we estimated the degree of centrality and betweenness centrality of the nodes. Nodes with centralities greater than 1 SD from the mean were defined as hubs of the network.

Histology

After the MRI study, brains were used for histological assessments. The brains were cryoprotected in 20% sucrose overnight and frozen. Frozen brains were cut on a cryostat at

40-μm thickness for the floating sections. The sections were incubated with primary antibodies overnight at room temperature. The following antibodies were used: anti-VGAT (1:1000 dilution; guinea pig polyclonal, Frontier Institute, Hokkaido, Japan), anti-Bassoon (1:1000 dilution; mouse monoclonal, SAP7F407, Enzo Life Sciences, Farmingdale, NY, USA), anti-ALFA (1:500 dilution; rabbit polyclonal, NanoTag, Göttingen, Germany), anti-NeuN (1:1000 dilution, rabbit monoclonal, EPR12763, Abcam, Cambridge, UK), anti-VGluT1 (1:1000 dilution; rabbit polyclonal, Frontier Institute), and anti-VGluT2 (1:1000 dilution; rabbit polyclonal, Frontier Institute). The sections were then treated with species-specific secondary antibodies conjugated to Alexa Fluor 488, 555, or 647 for 2 h at room temperature. Mounting medium (ProLong Glass Antifade Mountain, Thermo Fisher Scientific, Waltham, MA, USA) was applied to the samples, and they were mounted with coverslips (thickness: No. 1, Matsunami Glass). Macro-fluorescence images were obtained using an inverted microscope (BZ-X710; Keyence, Osaka, Japan). Micro-fluorescence images were obtained using super-resolution microscopy (SRM).

Super-resolution microscopy

Structured illumination microscopy (SIM)-SRM micro images were obtained using a Zeiss ELYRA 3D-SIM system equipped with an EM-CCD camera (Carl Zeiss). Before obtaining the SIM-SRM images, precise alignment for the different wavelengths of light was performed using the same mounting medium (ProLong Glass) containing 0.1% Tetraspeck (0.2-μm beads, Thermo Fisher Scientific) to correct for unavoidable laser misalignment and optical aberrations, which can cause the alignment not to coincide at high resolution. Next, 14–20 z-section images were obtained at intervals of 130 nm using a 64× objective lens. The number of pattern rotations of the structured illumination was adjusted to three in the ELYRA system. After obtaining all images, the SIM images were reconstructed and aligned using the channel alignment data.

Analysis of SRM images

SRM images were obtained as previously described[11] and analyzed using ImageJ software (http://rsb.info.nih.gov/ij/). The optimal brightness and grayscale pixel values were manually determined to provide the sharpest discrimination of the microstructure border. These adjusted images were then converted into binary images. To calculate the density of $VGAT^+$, $VGLuT1^+$, $VGluT2^+$, or $Bassoon^+$ puncta, SRM images of each type of staining were

randomly obtained at three locations each within the GPe, VP, MD, and LHb. The numbers of puncta were counted, and the mean number over the three locations was calculated. To calculate puncta size, 3D-SRM images of each type of staining were randomly obtained at three locations in each region. We observed the 3D image and used the single plane at which the size was largest to calculate the size. We measured the area of 150 puncta from each of the three locations. The mean size of the 150 puncta was used as the representative puncta size for each animal. To calculate the size of the $NeuN^+$ soma of GPe and VP neurons, 3D-SRM images of NeuN staining were randomly obtained within the GPe and VP. We observed the 3D image and used the single plane at which the size was largest to calculate the size. We calculated the size of 20–30 somas per mouse and used the average size as the representative soma size for each animal.

Mass spectrometry imaging

The procedures were previously described[11]. Mice were deeply anesthetized with a mixture of 0.3 mg/kg medetomidine, 4 mg/kg midazolam, and 5 mg/kg butorphanol, and the brains were rapidly removed from the skull and frozen in liquid N_2. Next, 10-μm-thick sections of fresh-frozen brains were prepared with a cryostat and thaw-mounted on conductive indium-tin-oxide-coated glass slides (Matsunami Glass). A pyrylium-based derivatization method was applied for the tissue localization imaging of neurotransmitters[17, 18]. TMPy (4.8 mg; Taiyo Nippon Sanso Co., Tokyo, Japan) was dissolved in a mixed solution (methanol:water:TEA=70:25:5) and was applied to brain sections using an airbrush (Procon Boy FWA Platinum 0.2-mm caliber airbrush, Mr. Hobby, Tokyo, Japan). To enhance the reaction efficiency of TMPy, TMPy-treated sections were placed into a dedicated container and allowed to react at 60°C for 10 min. The container included two channels in the central partition to wick moisture from the wet filter paper region to the sample section region. The filter paper was soaked with 1 mL of methanol/water (70%/30% volume/volume) and placed next to the section inside the container, which was then completely sealed to maintain humidity levels. The TMPy-labeled brain sections were sprayed with matrix (2,5-dihydroxybenzoic acid in 70% ethanol) using an automated pneumatic sprayer (TM-Sprayer, HTX Tech., Chapel Hill, NC, USA). Ten passes were performed according to the following conditions: flow rate, 120 μL/min; airflow, 10 psi; nozzle speed, 1100 mm/min.

To detect the laser spot area, the sections were scanned, and laser spot areas (200 shots) were detected with a spot-to-spot center distance of 80 μm. Signals between *m*/*z* 100–

650 were corrected. The section surface was irradiated with yttrium aluminum garnet laser shots in the positive ion detection mode using matrix-assisted laser desorption/ionization time-of-flight mass spectrometry (MALDI-TOF MS; timsTOF fleX, Bruker Daltonics, Bremen, Germany). The laser power was optimized to minimize the in-source decay of targets. The mass spectrometry spectra obtained were reconstructed to produce mass spectrometry images using Scils Lab software (Bruker Daltonics). Optical images of brain sections were obtained using a scanner (GT-X830, Epson, Tokyo, Japan), followed by MALDI-TOF MS of the sections. The detected mass of TMPy-labeled standard GABA (*m*/z 208.163) was increased by 105.0 Da compared with the original mass (molecular weight 103.0 Da). Tandem mass spectrometry was used to confirm the fragmentation ions of TMPy from the standard sample. A fragmented ion of the pyridine ring moiety (*m/z* 122.1) was regularly cleaved and observed for all TMPy-modified target molecules.

Statistical analysis

Statistical processing was performed using MATLAB. Two-tailed Student's t-tests were performed to compare treated and control mice. Bonferroni corrections were applied to correct p-values for multiple comparisons. Values are shown as the mean and standard error of the mean and are plotted as scatter diagrams.

Results

The pallidum is a common region for antidepressant-mediated volume increases.

To identify common structural plasticity changes after antidepressant treatment, we treated mice with antidepressants at concentrations and times that have previously demonstrated antidepressant effects, including the SSRI escitalopram (daily administration for 3 weeks, 15 mg/kg) [7], *R*-ketamine, *S*-ketamine, racemic (*SR*) ketamine (single injection, 10 mg/kg) [7], or psilocin (single injection, 1 mg/kg) [8] (Fig. 1A). We then conducted structural MRI and unbiased, brain-wide volumetric analysis known as voxel-based morphometry (VBM).

After 3 weeks of repeated SSRI treatment, volumes of the ventral striatum, including the nucleus accumbens (NAc), and striatal projection regions, such as the external globus pallidus (GPe), VP, substantia nigra pars reticulata (SNr), and entorhinal cortex (ENT), were increased. Conversely, volumes of the lateral habenula (LHb) and the mediodorsal thalamus (MD) were decreased (Fig. 1B). Surprisingly, a single injection of ketamine or psilocin induced similar volumetric changes in these regions (Fig. 1C–F).

Across all antidepressants, common volumetric changes included increases in NAc, VP, GPe, and ENT volumes, as well as decreases in MD volume (Fig. 1H and Supplementary Fig. 1). ROI-based volumetric analyses confirmed these results (Supplementary Fig. 2). Plotting the volume values for the GPe and VP further supported significant volume increases with all antidepressant treatments (Fig. 1I).

Next, to examine whether these antidepressant-associated volumetric changes were distinctive, we compared them with the volumetric changes observed after electroconvulsive stimulation (ECS), an animal model of electroconvulsive therapy (ECT) [10, 19]. After 9 sessions of ECS over 3 weeks, a volume increase was observed mainly within the hippocampus (Fig. 1G), suggesting that the volumetric changes induced by antidepressants and ECS are distinct. Taken together, these results indicate that the pallidum volume increases are a common effect of various antidepressants. We focused on the pallidum for further histological analysis.

Hypertrophy of VGAT-positive MSN terminals and increased GABA levels are common microstructural and molecular changes in antidepressant-treated mice.

We next investigated the molecular and anatomical basis for the increase in pallidal volume. We previously demonstrated that the VGAT expression level in dorsal striatal MSNs determines the size of their axon terminals (presynaptic structure) and the size of connecting neuron soma and dendrites (postsynaptic structure) [11]. Additionally, the convergence of such

microstructural changes led to MRI-detectable changes in GPe volume. Considering the analogy between ventral and dorsal striatal projections, we examined the inhibitory pre- and postsynaptic structures in both the VP and GPe after antidepressant treatments using SRM (Fig. 2A, B). All classes of antidepressants induced increases in the size and density of $VGAT^+$ puncta (presynaptic, Fig. 2C, D and Supplementary Fig. 3A, B), suggesting that VGAT was overexpressed in MSNs. They also induced an increase in $NeuN^+$ soma size in the VP and GPe principal neurons (Fig. 2E and Supplementary Fig. 3C). Additionally, we observed some structural changes in the excitatory presynapses in the GPe and VP (Supplementary Fig. 4). However, these alterations are unlikely to involve macroscopic volume changes due to the low punctal density.

Our previous research showed that MSN terminal hypertrophy is coupled with increased GABA levels [11]. Therefore, we hypothesized that antidepressants might similarly increase GABA levels in the basal ganglia. Using imaging mass spectrometry (IMS), we quantified GABA levels. As expected, treatment with all classes of antidepressants resulted in increased GABA content in the striatum, GPe, and VP (Fig. 3B). These results indicate that all antidepressants commonly induce VGAT overexpression, MSN terminal hypertrophy, and increased GABA levels.

Building on our prior research [11], we hypothesized that striatal VGAT overexpression results in enhanced GABA levels and hypertrophy of the MSN terminals. To confirm this, we injected an AAV vector expressing ALFA-tagged VGAT into the striatum (Fig. 3C) and compared GABA content between AAV injection and no-injection sides. Striatal overexpression of VGAT in MSNs resulted in an increase in GABA content in the MSN termination area (Fig. 3D, E). We compared the sizes of ALFA-negative and ALFA-positive VGAT puncta (Fig. 3F). Striatal overexpression of VGAT in MSNs resulted in an increase in the size of $VGAT^+$ puncta and the $Bassoon^+$ presynaptic active zone (Fig. 3G, H). These results suggest that all antidepressants commonly induce increased GABA levels and MSN terminal hypertrophy through VGAT overexpression in MSNs.

Antidepressants can be divided into two subtypes based on the patterns of volumetric change they induce.

Using principal component analysis (PCA) and hierarchical clustering on the brain volume change patterns of the ECS and various antidepressant treatments compared with those of the control group, we found distinct differences between the antidepressant group and the ECS

group (Fig. 4A, B). This result supported the distinctive features of antidepressant treatment and ECS (Fig. 1B–G). Despite the similarity among antidepressants, PCA identified two subgroups of antidepressant-mediated volumetric changes (Fig. 4A, B). The type I group included SSRIs and *S*-ketamine, while the type II group included *SR*-ketamine, *R*-ketamine, and psilocin. This classification was supported further by the post hoc ROI-based analysis of the overlapping area assessment (Supplementary Fig. 2).

When examining the volumetric changes in the GPe and VP, we found that the enlargement indices (fold change relative to each control) of brain volume in the VP were greater than those in the GPe after treatment with type II medications (psilocin, *R*-ketamine, and *SR*-ketamine) and vice versa (Fig. 1I and Fig. 4C). Interestingly, this macroscopic property was consistent with the microscopic property of MSN terminals but not soma size in both the VP and GPe principal neurons (Fig. 2C–E and Fig. 4D–F). This observation indicates that the type II group potentiates ventral MSN terminal hypertrophy, while the type I group potentiates dorsal MSN terminal hypertrophy.

Volumetric structural covariance analysis highlights the NAc–VP–MD/LHb pathway. The VP mainly receives inhibitory inputs from the NAc and projects to the MD and LHb [20-22]. In particular, the VP–LHb pathway has been implicated in depression [21, 23] and its antidepressant effect [21, 24]. The GPe also receives inhibitory input mainly from the dorsal striatum and projects to the GPi and SNr. Our VBM analysis suggested that the volume increases in the VP and GPe act as “hub regions” in the context of antidepressant responses. To investigate this possibility, we conducted a structure covariance network analysis [14, 15], which allowed an unbiased examination of the correlation between volumetric changes in paired regions (Fig. 5A). From these correlation matrices and network analyses, we found that the VP and MD were common hub regions in response to all classes of antidepressants (Fig. 5B). The GPe was not identified as a hub region.

Next, to assess the relevance of volumetric changes in the VP, we conducted a target ROI-based structure covariance analysis between the VP and known connecting regions, including the dorsal striatum, caudate putamen (CPu), NAc, central amygdala (CeA), basolateral amygdala (BLA), GPe, MD, LHb, lateral hypothalamic area (LHA), lateral preoptic area (LPO), substantia nigra pars reticulata (SNr), ventral tegmental area (VTA), and midbrain reticular nucleus (MRN) [21, 25]. According to this VP-centered analysis, the changes in structural covariances (Pearson correlation coefficients) in the control group were greatest

for the VP–MD across all antidepressants (Fig. 5C, E). By contrast, the changes were more modest for the NAc–VP and the VP–LHb (Fig. 5C, D, F). These results suggest that antidepressant treatment strengthens structural connectivity within the NAc–VP–MD or NAc–VP–LHb pathways.

Next, we analyzed structural changes in the MD and LHb to support the observed volumetric reductions, focusing on excitatory type I/II vesicular glutamate transporter $(VGluT1/2)^+$ and inhibitory $VGAT^+$ presynaptic structures (Fig. 6A, B). We found that across all antidepressants, the density but not the size of the $VGAT^+$ puncta, decreased in the MD and LHb (Fig. 6C, D). Additionally, in the MD, the density but not the size of $VGluT1^+$ puncta, decreased with psilocin and *R*-ketamine treatment (Fig. 6E, F). No structural changes were observed in the $VGluT2^+$ puncta after treatment with any antidepressant (Fig. 6G, H). These results indicate a common reduction in inhibitory terminals in the MD and LHb across all antidepressants, supporting the volumetric reductions observed in these regions.

Antidepressant treatment increased dopamine levels in the basal ganglia.

Because IMS can provide a comprehensive analysis of neurotransmitters, we also examined the 5-HT, glutamate, and dopamine content from the same section. Surprisingly, the dopamine content in the striatum was upregulated after antidepressant treatment (Supplementary Fig. 6A, B). In addition, the glutamate content in the basal ganglia was not altered by any antidepressants (Supplementary Fig. 6D, D). Although SSRIs and psilocin are 5-HT-related antidepressants, the 5-HT content in the basal ganglia was not altered by any antidepressants (Supplementary Fig. 6E, F). These results indicate that antidepressant treatment increased dopamine (DA) levels and GABA levels in the basal ganglia.

Discussion

This study demonstrated that the pallidal volume increase was a shared structural footprint of antidepressant treatment and that this increase was accountable for the enlargement of the MSN terminals with VGAT overexpression. Neurochemical analysis by IMS demonstrated an increase in GABA levels after antidepressant treatment. Artificial VGAT overexpression in MSNs was sufficient to reproduce the MSN terminal hypertrophy and an increase in GABA levels. Since we previously demonstrated that VGAT overexpression in MSNs enhanced GABA transmission at the pallidum [11], our findings suggest that a common mechanism of action of antidepressants involves enhanced GABA-mediated pallidal inhibition.

Structural covariance analysis revealed a potential link between the pallidus and the downstream structure. The VP is an output nucleus of the basal ganglia and projects to various regions to regulate motivated behavior, hedonic states, reinforcement, and reward and aversion processing [20-22, 25]. Therefore, antidepressant-induced VP inhibition can technically affect all projected regions. However, antidepressant treatments commonly resulted in a decrease in the selective volume of MD/LHb and an increase in the volume of the VP (Fig. 5E, F). The highlight of LHb is intriguing because it is well accepted that increased LHb activity causes a depressive state and that SSRIs and ketamine suppress LHb activity [21, 23]. We need to acknowledge that the causal relationship between the suppression of LHb activity and the decrease in LHb volume is currently unknown, and we only identified that the antidepressant-induced decrease in LHb volume coincides with decreased inhibitory presynapse density but not with decreased excitatory presynaptic density (Fig. 6). Such histological data imply the disinhibition of LHb activity after antidepressant treatment, which seems contradictory to the prevailing view [21, 23]. To understand the functional and structural consequences of LHb more fully, at the very least, analyses of animal models of depression subjected to antidepressant treatments are required. In addition, the engagement of VP–LHb monosynaptic or polysynaptic connections should be clarified to determine the relevance of the NAc–VP–LHb pathway.

VP projections to the MD are important for the cognitive component of reward learning [26], and MD activity is associated with stress resilience in mice [27], indicating the role of MD in depression pathophysiology. Human imaging studies have demonstrated a decrease in MD volume in individuals with stress-related disorders, including depression [28] and posttraumatic stress disorder [29]. However, other thalamic nuclei in addition to the MD showed a decreased volume in these disorders. The antidepressant effect on thalamic volume was

specific to the MD in mice, suggesting a distinct mechanism for the decrease in MD volume after antidepressant treatment. The biological importance of the decreased MD volume and the NAc–VP–MD pathway could be addressed by the abovementioned approach as it was for the LHb.

Based on the patterns of volume increase in the GPe and VP, we found that antidepressants can be divided into two subgroups. This subdivision is not only reflected in brain volume changes but also coupled with structural changes in MSN terminals (Fig. 4). It should be noted that the subdivisions clearly separated the chronic volumetric effects by *R*- or *S*-ketamine. Previous studies supported this distinction; functional MRI studies with rats showed distinct acute activation patterns between *R*-ketamine and *S*-ketamine [30]. [^{18}F]-Fluorodeoxyglucose positron emission tomography of human brains revealed a distinct acute metabolic pattern between *R*-ketamine and *S*-ketamine [31]. c-Fos mapping with mouse brains also revealed distinct activation patterns between *R*-ketamine and *S*-ketamine [32]. Although the difference in the sustained effects is not clear in humans, *R*-ketamine showed more sustained antidepressant effects than *S*-ketamine in animals [9]. Combined with the sustained antidepressant effect of psilocybin in humans [4], the grouping with *R*-ketamine and psilocin may be related to their long-term effects. In contrast, the grouping with SSRIs and *S*-ketamine may not be.

We commonly observed a delayed increase in dopamine content in the basal ganglia across all antidepressants (Supplementary Fig. 6A, B). Previous studies have shown that ketamine and psilocin acutely increase extracellular dopamine concentrations in the mPFC, NAc, hippocampus, and amygdala by activating serotonin and glutamate neurons [33, 34]. However, our results did not show a chronic increase in serotonin or glutamate content in the basal ganglia. Notably, the dopamine content differed from the extracellular dopamine concentration, indicating that addressing dopamine synthesis and metabolism rather than monitoring dopamine neuron activity is necessary for antidepressant treatment. The relevance of increased dopamine content in the basal ganglia has remained unclear, but it is expected to clarify whether chronic increases in dopamine content are related to antidepressant effects.

In summary, we discovered shared structural and molecular changes after antidepressant treatments. An increase in pallidal volume may serve as a structural biomarker indicating the efficacy of antidepressants. The antidepressant-induced increase in GABA-mediated inhibition of the pallidum can be attributed to VP-targeted neuromodulation to mimic the therapeutic effect. An increased GABA content in the globus pallidus may serve as

a therapeutic biomarker that can be detected using magnetic resonance spectroscopy.

Acknowledgments

We thank Collaborative Research Resources, Keio University School of Medicine, for technical assistance with the Zeiss ELYRA 3D-SIM system. We also thank Lisa Kreiner, PhD, from Edanz (https://jp.edanz.com/ac) for editing the English text of a draft of this manuscript.

Funding

This work was supported by a Grant-in-Aid from the Japan Society for the Promotion of Science (JSPS) KAKENHI Grant Number JP22K15215 (Y.A.), the Takeda Science Foundation (Y.A.), the Astellas Foundation for Research on Metabolic Disorders (Y.A.), and grants from Brain Mapping by Integrated Neurotechnologies for Disease Studies (Brain/MINDS) by the Japan Agency for Medical Research and Development (AMED) under grant numbers 23zf0127007s0102 (Y.S.), JP23zf0127003 (Y.S.), JP23gm1210009 (Y.S.), JP19dm0207069 (K.F.T), JP21wm0525018 (S.Y.), and JP24wm0625001 (S.Y.).

Author contributions

K.F.T. supervised the project; Y.A. and K.F.T. designed the experiments; Y.A. and S.Y. performed and analyzed the MRI studies; Y.A. performed and analyzed the histological assessments; Y.A., R.M., S.T., and Y.S. performed and analyzed the imaging mass spectroscopy; K.Y. and D.I. provided psilocin; K.H. provided ketamine; and Y.A. and K.F.T. wrote and revised the original manuscript.

Competing interests

Dr. Hashimoto is the inventor of and has filed patent applications for “The use of *R*-ketamine in the treatment of psychiatric diseases,” “(*S*)-norketamine and salt thereof as a pharmaceutical,” “*R*-ketamine and derivatives thereof as prophylactic or therapeutic agents for neurodegenerative disease or recognition function disorder,” “Preventive or therapeutic agent and pharmaceutical composition for inflammatory diseases or bone diseases,” “*R*-ketamine and its derivatives as a preventive or therapeutic agent for a neurodevelopmental disorder,” and “TGF-β1 in the treatment of depression” by Chiba University. The other authors declare that they have no competing interests.

Data availability

All data are available in the main text or the supplementary materials. Materials, resources, plasmids, and reagents are available from the corresponding author upon request.

References

1. Jakobsen JC, Katakam KK, Schou A, Hellmuth SG, Stallknecht SE, Leth-Moller K *et al.* Selective serotonin reuptake inhibitors versus placebo in patients with major depressive disorder. A systematic review with meta-analysis and Trial Sequential Analysis. *BMC Psychiatry* 2017; **17**(1)**:** 58.

2. Abdallah CG, Sanacora G, Duman RS, Krystal JH. Ketamine and rapid-acting antidepressants: a window into a new neurobiology for mood disorder therapeutics. *Annu Rev Med* 2015; **66:** 509-523.

3. Zarate CJ, Singh J, Carlson P, Brutsche N, Ameli R, Luckenbaugh D *et al.* A randomized trial of an N-methyl-D-aspartate antagonist in treatment-resistant major depression. *Arch Gen Psychiatry* 2006; **63**(8)**:** 856-864.

4. Gukasyan N, Davis AK, Barrett FS, Cosimano MP, Sepeda ND, Johnson MW *et al.* Efficacy and safety of psilocybin-assisted treatment for major depressive disorder: Prospective 12-month follow-up. *J Psychopharmacol* 2022; **36**(2)**:** 151-158.

5. Shirota O, Hakamata W, Y G. Concise large-scale synthesis of psilocin and psilocybin, principal hallucinogenic constituents of "magic mushroom". *J Nat Prod* 2003; **66**(6)**:** 885-887.

6. Zhang JC, Li SX, Hashimoto K. R (-)-ketamine shows greater potency and longer lasting antidepressant effects than S (+)-ketamine. *Pharmacol Biochem Behav* 2014; **116:** 137-141.

7. Yoshida K, Drew MR, Kono A, Mimura M, Takata N, Tanaka KF. Chronic social defeat stress impairs goal-directed behavior through dysregulation of ventral hippocampal activity in male mice. *Neuropsychopharmacology* 2021; **46**(9)**:** 1606-1616.

8. Shao LX, Liao C, Gregg I, Davoudian PA, Savalia NK, Delagarza K *et al.* Psilocybin induces rapid and persistent growth of dendritic spines in frontal cortex in vivo. *Neuron* 2021; **109**(16)**:** 2535-2544 e2534.

9. Yang C, Shirayama Y, Zhang JC, Ren Q, Yao W, Ma M *et al.* R-ketamine: a rapid-onset and sustained antidepressant without psychotomimetic side effects. *Transl Psychiatry* 2015; **5**(9)**:** e632.

10. Abe Y, Yokoyama K, Kato T, Yagishita S, Tanaka KF, Takamiya A. Neurogenesis-independent mechanisms of MRI-detectable hippocampal volume increase following electroconvulsive stimulation. *Neuropsychopharmacology* 2024.

11. Abe Y, Yagishita S, Sano H, Sugiura Y, Dantsuji M, Suzuki T *et al.* Shared GABA transmission pathology in dopamine agonist- and antagonist-induced dyskinesia. *Cell Reports Medicine* 2023; **4:** 101208.

12. de Guzman AE, Wong MD, Gleave JA, Nieman BJ. Variations in post-perfusion immersion fixation and storage alter MRI measurements of mouse brain morphometry. *Neuroimage* 2016; **142:** 687-695.

13. Barrière DA, Ella A, Szeremeta F, Adriaensen H, Même W, Chaillou E *et al.* Brain orchestration of pregnancy and maternal behavior in mice. *bioRxiv* 2020.

14. Yee Y, Ellegood J, French L, Lerch JP. Organization of thalamocortical structural covariance and a corresponding 3D atlas of the mouse thalamus. *Neuroimage* 2024; **285:** 120453.

15. Wannan CMJ, Cropley VL, Chakravarty MM, Bousman C, Ganella EP, Bruggemann JM *et al.* Evidence for Network-Based Cortical Thickness Reductions in Schizophrenia. *Am J Psychiatry* 2019; **176**(7)**:** 552-563.

16. Tsugawa S, Honda S, Noda Y, Wannan C, Zalesky A, Tarumi R *et al.* Associations Between Structural Covariance Network and Antipsychotic Treatment Response in Schizophrenia. *Schizophr Bull* 2023.

17. Shikano H, Ikeda A, Maejima Y, Kobayashi S, Terauchi T, Yokoyama J *et al.* Optimization of the use of Py-Tag for next generation derivatization reagents in imaging mass spectrometry. *J Biosci Bioeng* 2022; **134**(3)**:** 264-268.

18. Taira S, Ikeda A, Sugiura Y, Shikano H, Kobayashi S, Terauchi T *et al.* Pyrylium based derivatization imaging mass spectrometer revealed the localization of L-DOPA. *PLoS One* 2022; **17**(8)**:** e0271697.

19. Takamiya A, Chung JK, Liang KC, Graff-Guerrero A, Mimura M, Kishimoto T. Effect of electroconvulsive therapy on hippocampal and amygdala volumes: systematic review and meta-analysis. *Br J Psychiatry* 2018; **212**(1)**:** 19-26.

20. Soares-Cunha C, Heinsbroek JA. Ventral pallidal regulation of motivated behaviors and reinforcement. *Front Neural Circuits* 2023; **17:** 1086053.

21. Knowland D, Lilascharoen V, Pacia CP, Shin S, Wang EH, Lim BK. Distinct Ventral Pallidal Neural Populations Mediate Separate Symptoms of Depression. *Cell* 2017; **170**(2)**:** 284-297 e218.

22. Li YD, Luo YJ, Xu W, Ge J, Cherasse Y, Wang YQ *et al.* Ventral pallidal GABAergic neurons control wakefulness associated with motivation through the ventral tegmental pathway. *Mol Psychiatry* 2021; **26**(7)**:** 2912-2928.

23. Yang Y, Cui Y, Sang K, Dong Y, Ni Z, Ma S *et al.* Ketamine blocks bursting in the lateral habenula to rapidly relieve depression. *Nature* 2018; **554**(7692)**:** 317-322.

24. Ma S, Chen M, Jiang Y, Xiang X, Wang S, Wu Z *et al.* Sustained antidepressant effect of ketamine through NMDAR trapping in the LHb. *Nature* 2023; **622**(7984)**:** 802-809.

25. Stephenson-Jones M, Bravo-Rivera C, Ahrens S, Furlan A, Xiao X, Fernandes-Henriques C *et al.* Opposing Contributions of GABAergic and Glutamatergic Ventral Pallidal Neurons to Motivational Behaviors. *Neuron* 2020; **105**(5)**:** 921-933 e925.

26. Leung BK, Balleine BW. Ventral pallidal projections to mediodorsal thalamus and ventral tegmental area play distinct roles in outcome-specific Pavlovian-instrumental transfer. *J Neurosci* 2015; **35**(12)**:** 4953-4964.

27. Li F, Zheng X, Wang H, Meng L, Chen M, Hui Y *et al.* Mediodorsal thalamus projection to medial prefrontal cortical mediates social defeat stress-induced depression-like behaviors. *Neuropsychopharmacology* 2024.

28. Chibaatar E, Watanabe K, Okamoto N, Orkhonselenge N, Natsuyama T, Hayakawa G *et al.* Volumetric assessment of individual thalamic nuclei in patients with drug-naive, first-episode major depressive disorder. *Front Psychiatry* 2023; **14:** 1151551.

29. Yang B, Jia Y, Zheng W, Wang L, Qi Q, Qin W *et al.* Structural changes in the thalamus and its subregions in regulating different symptoms of posttraumatic stress disorder. *Psychiatry Res Neuroimaging* 2023; **335:** 111706.

30. Masaki Y, Kashiwagi Y, Watabe H, Abe K. (R)- and (S)-ketamine induce differential fMRI responses in conscious rats. *Synapse* 2019; **73**(12)**:** e22126.

31. Vollenweider FX, Leenders KL, Øye I, Hell D, Angst J. Differential psychopathology and patterns of cerebral glucose utilisation produced by (S)- and (R)-ketamine in healthy volunteers using positron emission tomography (PET). *Eur Neuropsychopharmacol* 1997; **7**(1)**:** 25-38.

32. Yokoyama R, Ago Y, Igarashi H, Higuchi M, Tanuma M, Shimazaki Y *et al.* (R)-ketamine restores anterior insular cortex activity and cognitive deficits in social isolation-reared mice. *Mol Psychiatry* 2024.

33. Wojtas A, Bysiek A, Wawrzczak-Bargiela A, Maćkowiak M, Gołembiowska K. Limbic System Response to Psilocybin and Ketamine Administration in Rats: A Neurochemical and Behavioral Study. *International Journal of Molecular Sciences* 2023; **25**(1).

34. Pham TH, Defaix C, Nguyen TML, Mendez-David I, Tritschler L, David DJ *et al.* Cortical and raphe GABAA, AMPA receptors and glial GLT-1 glutamate transporter contribute to the sustained antidepressant activity of ketamine. *Pharmacology Biochemistry and Behavior* 2020; **192**.

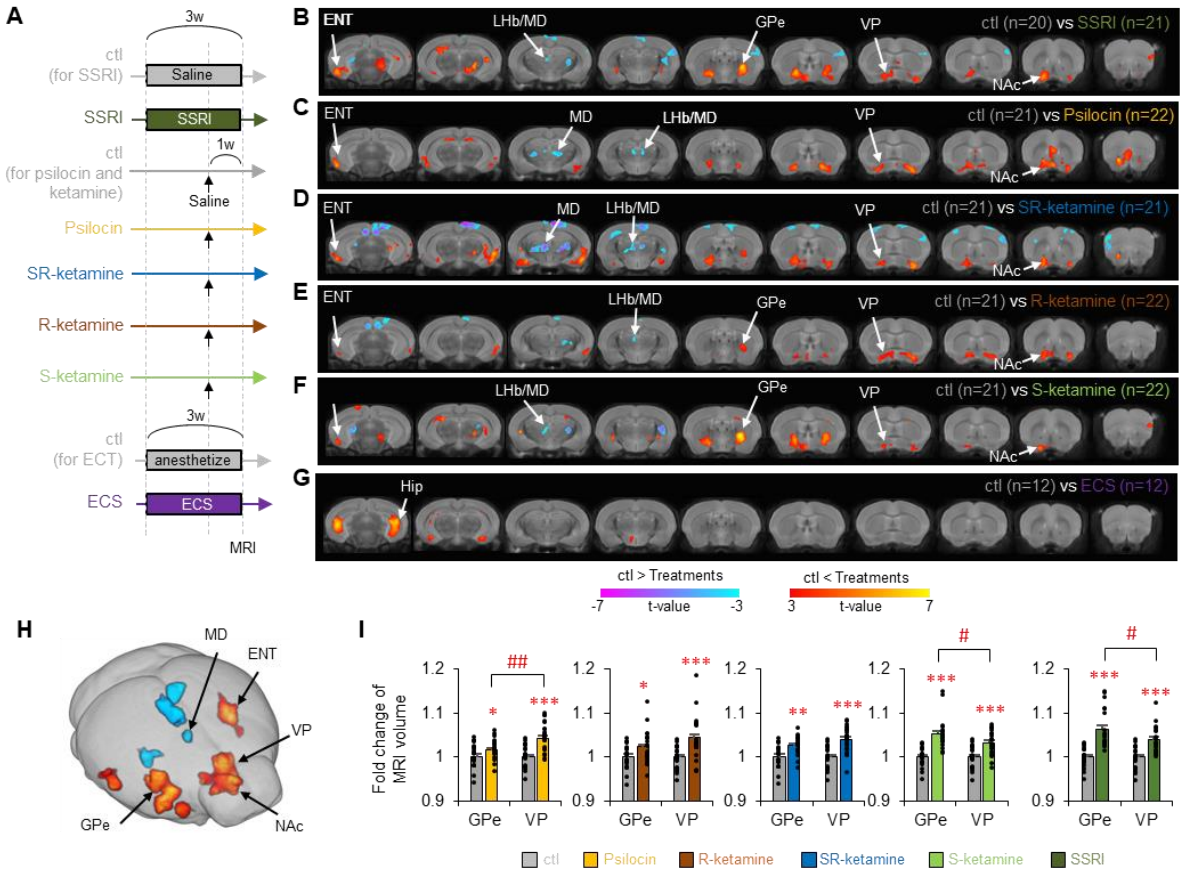

Fig. 1: The pallidum is a common region for antidepressant-mediated volume increases in mice.

(A) Experimental time course for the administration of saline, psilocin, ketamine, escitalopram (SSRI), or electroconvulsive stimulation (ECS). (B–G) Voxel-based analysis of brain volume differences between treated mice and the appropriate control mice (ctl). Hot colors indicate significant volume increases compared with those in the ctls (family-wise error corrected $p < 0.05$), and cool colors indicate the opposite. (H) Volume changes in overlapping regions of the brain after treatment. Red indicates commonly increased volumes, and blue indicates commonly decreased volumes. (I) Fold changes in the brain volume of the globus pallidus (GPe) and ventral pallidum (VP) after each antidepressant treatment. *$p < 0.05$, **$p < 0.01$, ***$p < 0.001$ (Student *t* tests were used for comparisons with ctls, and *p* values are adjusted with post hoc Bonferroni corrections for multiple comparisons). #$p < 0.05$, ##$p < 0.01$ (Student *t* tests were used for comparisons between the GPe and VP of the treated mice, *p* values are presented with post hoc Bonferroni corrections). ENT, entorhinal cortex; Hip, hippocampus; LHA, lateral hypothalamus area; LHb, lateral habenula; MD, mediodorsal nucleus of the thalamus; NAc, nucleus accumbens.

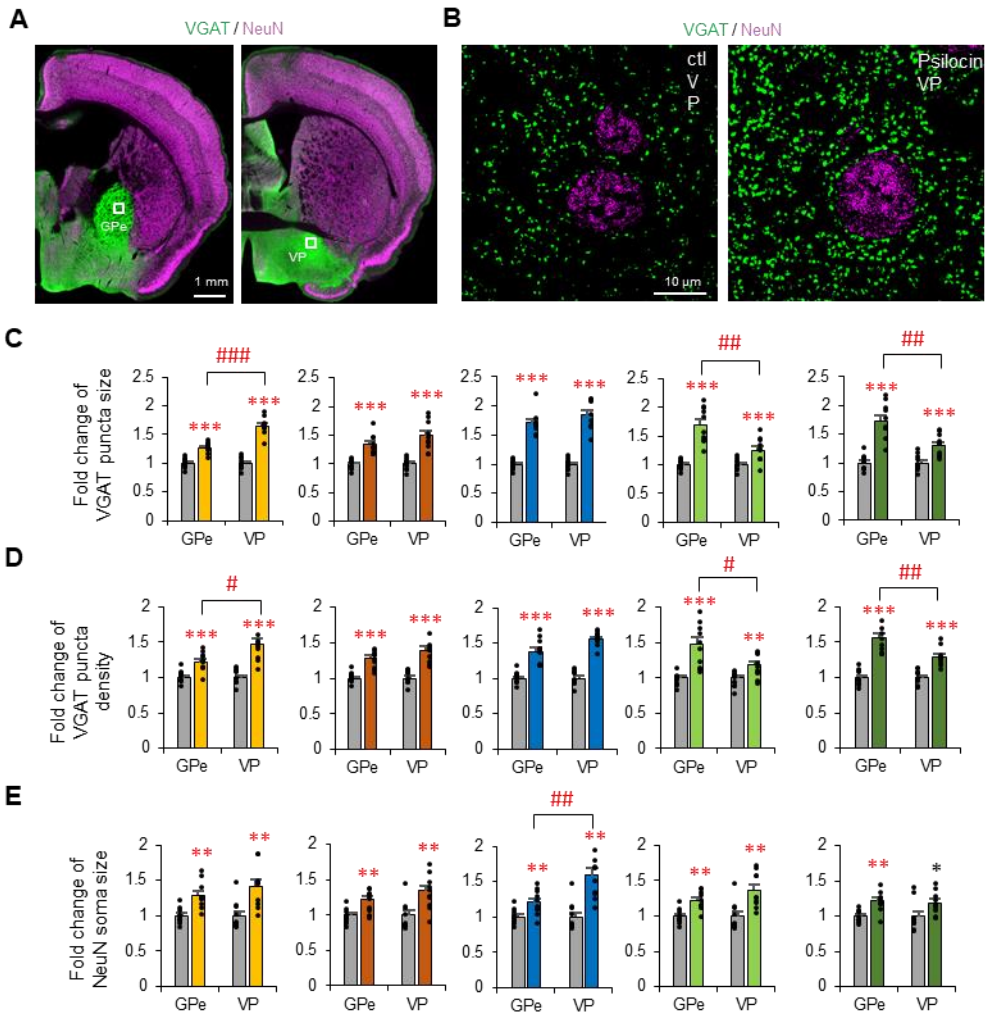

Fig. 2: Hypertrophy of MSN terminals and pallidal neuron somas is a common microstructural change in antidepressant-treated mice.

(A) Representative microscopy images including the globus pallidus (GPe) and the ventral pallidum (VP). The vesicular γ-aminobutyric acid (GABA) transporter (VGAT) and neuronal nuclei (NeuN) are labeled in green and magenta, respectively. (B) Representative super-resolution microscopy images of VGAT and NeuN staining in the VP of control (ctl) and psilocin-treated mice. (C–E) Fold changes in the size and density of VGAT puncta in medium spiny neuron (MSN) terminals and in the size of GPe/VP neuronal soma after antidepressant treatment (n = 10 mice for each treatment). *$p < 0.05$, **$p < 0.01$, ***$p < 0.001$ (Student *t* tests were used for comparisons with each ctl, and *p* values are presented with post hoc Bonferroni corrections for multiple comparisons). #$p < 0.05$, ##$p < 0.01$, ###$p < 0.001$ (Student *t* tests were used for comparisons between the GPe and VP of the treated mice, *p* values are presented with post hoc Bonferroni correction). The values are plotted as the means ± standard errors of the means.

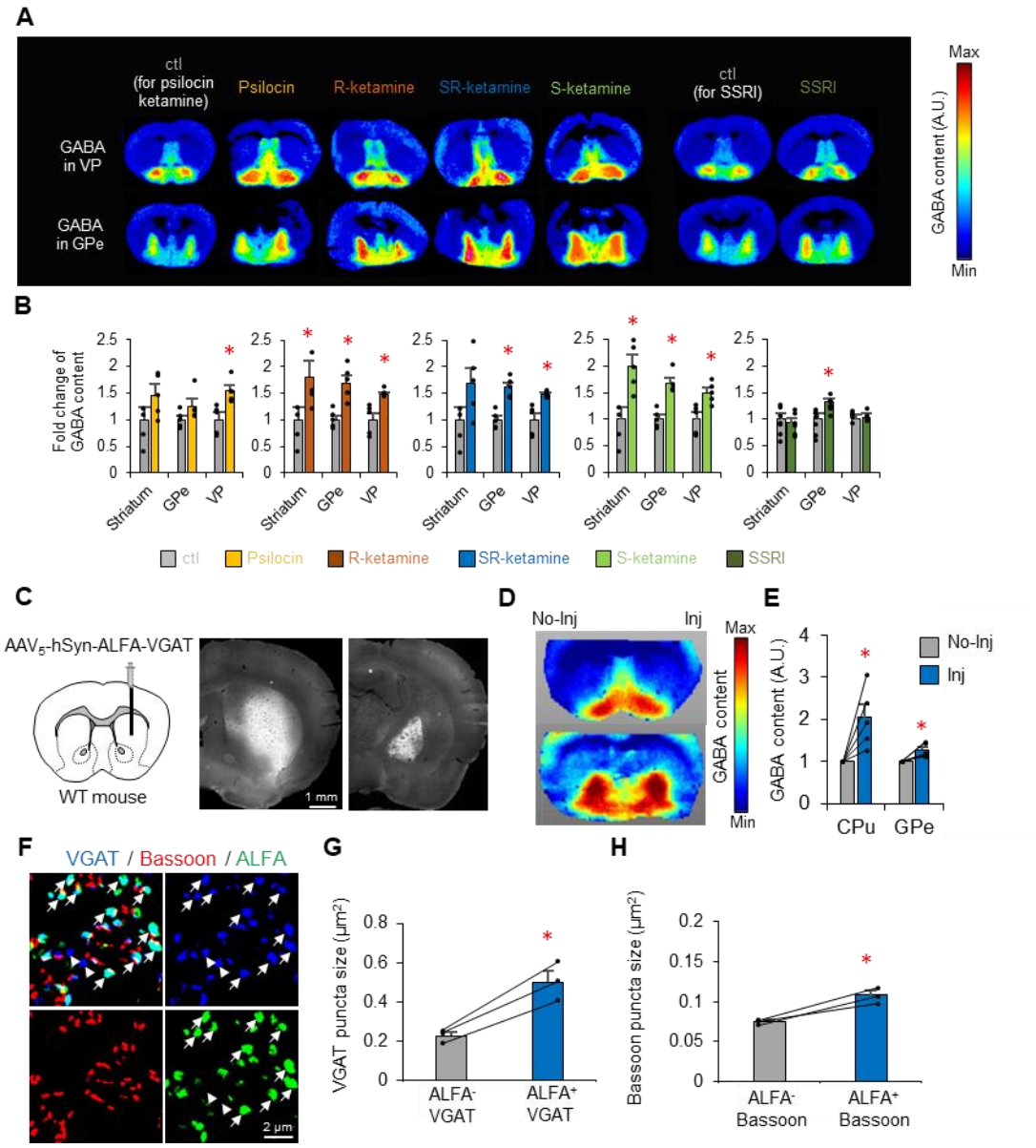

Fig. 3: Striatal overexpression of VGAT induced a shared biochemical responses of increased pallidal GABA content and enlargement of MSN terminals.

(A) Representative imaging mass spectrometry (IMS) images of γ-aminobutyric acid (GABA) in the globus pallidus (GPe) and the ventral pallidum (VP) of treated and control (ctl) mice. (B) Fold changes in GABA content based in the striatum, GPe, VP, and ctl are plotted. GABA content in the basal ganglia was increased after the indicated antidepressant treatments (n = 5 mice for each treatment). (C) The adeno-associated virus (AAV) plasmid construct pAAV-hSyn-ALFA-VGAT-pA was injected into the dorsal striatum of wild-type (WT) mice. Representative image of ALFA staining. (D) Representative imaging mass spectrometry of GABA content in VGAT-overexpressing mice. (E) GABA content in the caudate putamen (CPu) and GPe were compared between the AAV-injected side (Inj) and the noninjected side

(No-Inj) (n = 5). (F) Representative super-resolution microscopy images of VGAT, Bassoon (presynaptic protein), and ALFA in the GPe. The arrows indicate VGAT overexpressing terminals, and the arrowheads indicate non-overexpressing terminals. (G, H) The sizes of VGAT and Bassoon puncta in medium spiny neuron (MSN) terminals were compared between $ALFA^{+}$ and $ALFA^{-}$ puncta in the GPe (n = 3). *$p < 0.05$ (Student *t* tests were used with *p* values adjusted with post hoc Bonferroni corrections for multiple comparisons). The values are plotted as the means ± standard errors of the means.

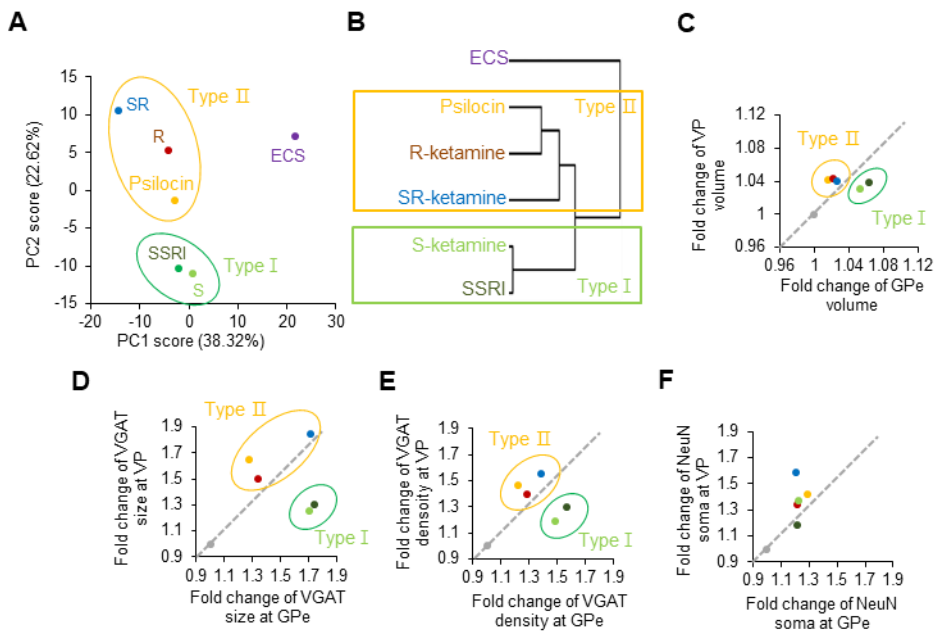

Fig. 4: Principal component analysis identified two subgroups of volumetric changes. (A, B) Principal component analysis and hierarchical clustering of volume changes in treated mice. (C) The scatter plots of the fold change in the volume of the globus pallidus (GPe) and the ventral pallidum (VP) show VP predominant volume increases (type II group, yellow circles) and GPe predominant volume increases (type I group, green circles). (D, E) Scatter plots of the fold changes in the vesicular γ-aminobutyric acid (GABA) transporter (VGAT) puncta size and density and neuronal nuclei (NeuN) soma size in the GPe and VP. SR, *SR*-ketamine; R, *R*-ketamine; ECS, electroconvulsive stimulation; SSRI, escitalopram.

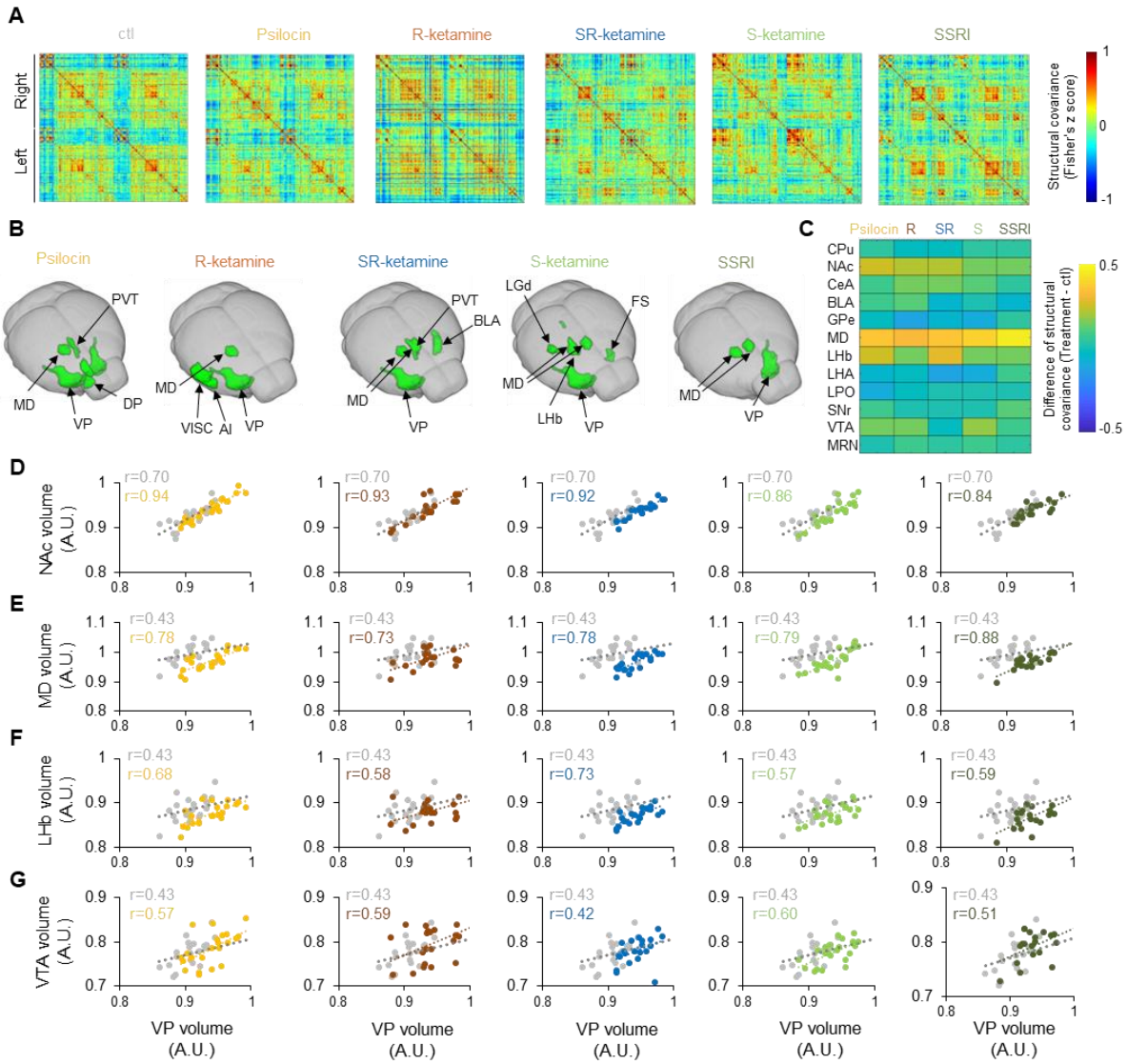

Fig. 5: Structural covariance analysis highlights the NAc–VP–MD/LHb pathway. (A) Region of interest (ROI)-based structural covariance matrices in antidepressant-treated mice. (B) Hub regions were calculated from structural covariance differences between treated and control (ctl) mice. The ventral pallidum (VP) and mediodorsal thalamus (MD) were common hub regions in all treated mice. (C) Differences in the structural covariance between the VP and connecting regions compared with those in ctl mice. (D–G) Plots of each brain volume and the VP volume in antidepressant-treated mice. Structural covariances of each region are shown as Pearson correlations (*r*). A.U., arbitrary units; AI, agranular insular cortex; BLA, basolateral amygdala; CeA, central amygdala; CPu, caudate putamen; DP, dorsal peduncular area; ENT, entorhinal cortex; FS, fundus of the striatum; GPe, globus pallidus, Hip, hippocampus; LGd, dorsal part of the lateral geniculate complex; LHA, lateral hypothalamus area; LHb, lateral habenula; LPO, lateral preoptic area; MRN, midbrain

reticular nucleus; NAc, nucleus accumbens; PVT, paraventricular nucleus of the thalamus; SNr, substantia nigra pars reticulata; SSRI, escitalopram; VISC, visual cortex; VTA, ventral tegmental nucleus.

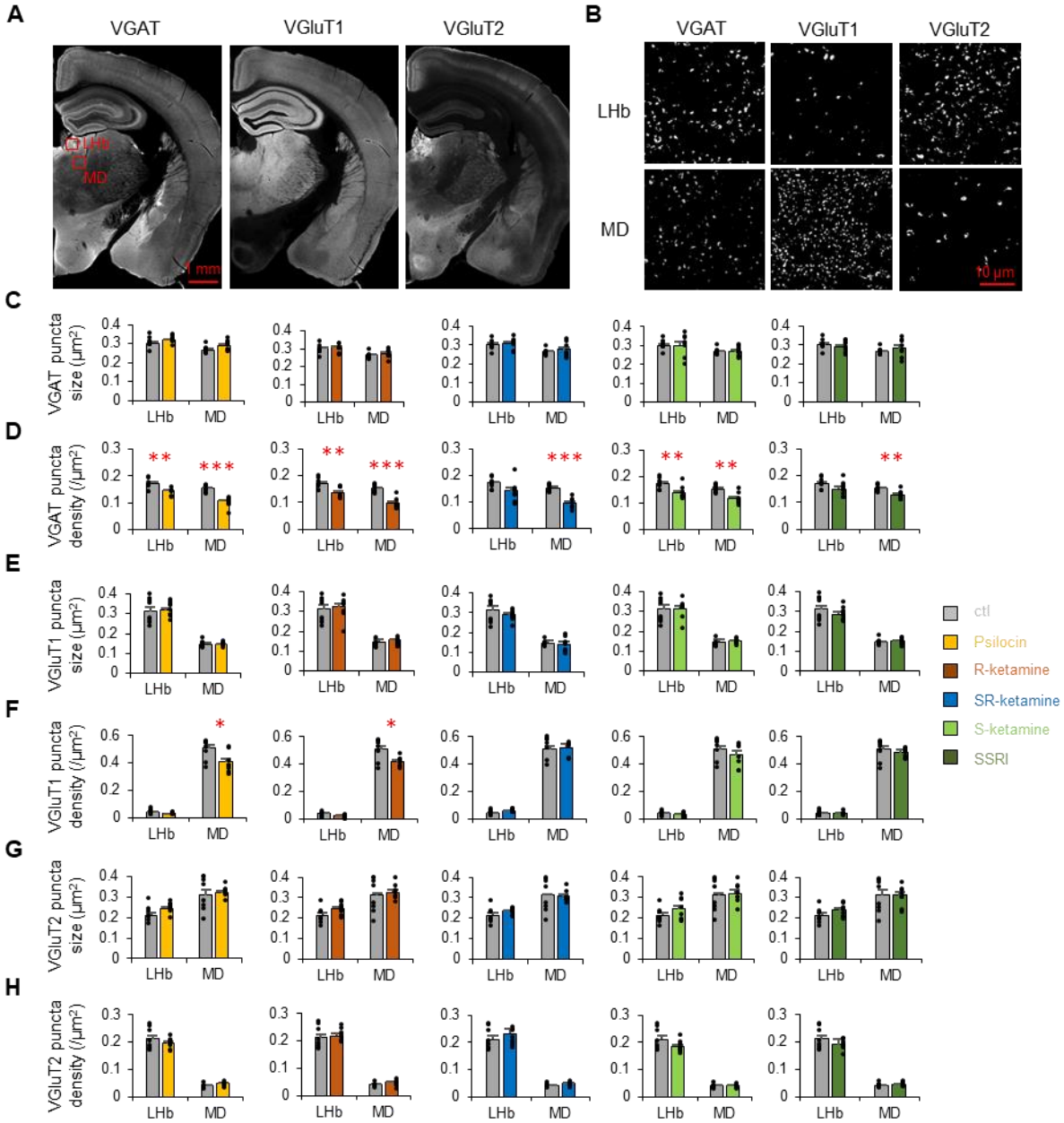

Fig. 6: Structural changes in inhibitory terminals in the LHb and MD of antidepressant-treated mice.

(A) Representative microscopy images of vesicular γ-aminobutyric acid (GABA) transporter (VGAT), type I vesicular glutamate transporter (VGluT1), and type II VGlu (VGluT2) staining. The red squares of the lateral habenula (LHb) and mediodorsal thalamus (MD) are shown after further super-resolution microscopy (SRM) analysis. (B) Representative SRM images of VGAT, VGluT1, and VGluT2 staining in the MD and LHb. (C–H) The size or density of VGAT, VGluT1, or VGluT2 puncta in the LHb and MD were compared between treated and control (ctl) mice (n = 8 mice for each treatment). *$p < 0.05$, **$p < 0.01$, ***$p <$

0.001 (Student *t* tests were used to compare treatment and ctls, *p* values are presented with post hoc Bonferroni corrections for multiple comparisons). The values are plotted as the means ± standard errors of the means. SSRI, escitalopram.